

Experimental investigation of closed-loop active control to modulate coherent structures by mu-level method

Jian-Xia Bai(白建侠), Zi-Ye Fan(范子椰), Nan Jiang(姜楠), Qiu-Ying Li(李秋营), and Xiao-Bo Zheng(郑小波)

Citation: Chin. Phys. B, 2024, 33 (**7**): 074701. DOI: 10.1088/1674-1056/ad3dc7
Journal homepage: http://cpb.iphy.ac.cn; http://iopscience.iop.org/cpb

What follows is a list of articles you may be interested in

Effect of pressure evolution on the formation enhancement in dual interacting vortex rings

Jianing Dong(董佳宁), Yang Xiang(向阳), Hong Liu(刘洪), and Suyang Qin(秦苏洋)
Chin. Phys. B, 2022, 31 (**8**): 084701. DOI: 10.1088/1674-1056/ac65f6

Effects of single synthetic jet on turbulent boundary layer

Jin-Hao Zhang(张津浩), Biao-Hui Li(李彪辉), Yu-Fei Wang(王宇飞), and Nan Jiang(姜楠)
Chin. Phys. B, 2022, 31 (**7**): 074702. DOI: 10.1088/1674-1056/ac4bd0

Coherent structures over riblets in turbulent boundary layer studied by combining time-resolved particle image velocimetry (TRPIV), proper orthogonal decomposition (POD), and finite-time Lyapunov exponent (FTLE)

Shan Li(李山), Nan Jiang(姜楠), Shaoqiong Yang(杨绍琼), Yongxiang Huang(黄永祥), Yanhua Wu(吴彦华)
Chin. Phys. B, 2018, 27 (**10**): 104701. DOI: 10.1088/1674-1056/27/10/104701

Predetermined control of turbulent boundary layer with a piezoelectric oscillator

Xiao-Bo Zheng(郑小波), Nan Jiang(姜楠), Hao Zhang(张浩)
Chin. Phys. B, 2016, 25 (**1**): 014703. DOI: 10.1088/1674-1056/25/1/014703

Experimental study on spectrum and multi-scale nature of wall pressure and velocity in turbulent boundary layer

Zheng Xiao-Bo (郑小波), Jiang Nan (姜楠)
Chin. Phys. B, 2015, 24 (**6**): 064702. DOI: 10.1088/1674-1056/24/6/064702

Experimental investigation of closed-loop active control to modulate coherent structures by mu-level method

Jian-Xia Bai(白建侠)[1], Zi-Ye Fan(范子椰)[2], Nan Jiang(姜楠)[2,4,†], Qiu-Ying Li(李秋营)[1], and Xiao-Bo Zheng(郑小波)[3]

[1] *Department of Mathematics, Tianjin Renai College, Tianjin* 301636, *China*
[2] *Institute of Mechanics, Department of Mechanics, School of Mechanical Engineering, Tianjin University, Tianjin* 300354, *China*
[3] *College of Energy and Power Engineering, Lanzhou University of Technology, Lanzhou* 730050, *China*
[4] *Tianjin Key Laboratory of Modern Engineering Mechanics, Tianjin* 300354, *China*

(Received 19 December 2023; revised manuscript received 26 February 2024; accepted manuscript online 12 April 2024)

The experimental research on zero-net-mass-flux jet closed-loop active control was conducted in the wind tunnel. The mu-level method successfully detected burst events of the coherent structures. The streamwise velocity signals in the turbulent boundary layer were measured by HWA. The drag reduction rate of 16.7% is obtained comparable to that of the open-loop control and saves 75% of the input energy at the asynchronous 100 V/160 Hz control case, which reflects the advantages of the closed-loop control. The experimental findings indicate that the intensity increases in the near-wall region. The perturbation of the PZT vibrators on the skewness factor is concentrated in the region $y^+ < 60$. The generation of high-speed fluids is depressed and the downward effect of high-speed fluids weakens. The alteration of energy distribution and the discernible impact of modulation between structures of varying scales are observed. The correlation coefficient exhibits a strong positive correlation, which indicates that the large-scale structures produce modulation effect on small-scale ones. The occurrence of burst events is effectively suppressed. The disturbance has the characteristics of stable periodicity, positive and negative symmetry, low intermittency, and high pulsation strength. The conditional phase waveform shows that the fluctuation amplitude increases, indicating amplitude modulation effects on coherent structures.

Keywords: turbulent boundary layer (TBL), burst event, coherent structures, mu-level method

PACS: 47.85.lb, 47.85.ld, 47.27.nb, 47.27.De **DOI:** 10.1088/1674-1056/ad3dc7

1. Introduction

Coherent structures play a key role in the formation, development, sustainment, and evolution of turbulence. Strip structures, large-scale motion, and super-large-scale motion were classified by Marusic *et al.*[1] into three categories depending on their scales, and it was discovered that different scales of coherent structures are located at various wall-normal positions of the turbulent boundary layer (TBL). Studies show the existence of modulation between coherent structures at various scales. Huchins *et al.*[2] discovered that there is a phenomenon where large-scale structures affect small-scale structures in the near-wall region. Ganapathisubramani *et al.*[3] identified that small-scale pulsation is subject to the frequency and amplitude modulation of large-scale pulsation in the TBL. Guala *et al.*[4] found that there is a significant interaction between large-scale structures in the atmospheric boundary layer and coherent structures across all scales, ranging from energetic vortex to dissipative scale. Hwang and Sung[5] found that the positive large scale strengthens the movement of the vortex structure and enhances the skin friction. In the meantime, the presence of negative large-scale pulsations serves to diminish the vortex motion and subsequently alleviate the skin friction.

The drag reduction mechanism primarily focuses on controlling coherent structures in order to address the strong correlation between high skin friction and coherent structures in the TBL.[6,7] Effectively interfering and modulating coherent structures by depressing the burst events and thus reducing skin friction is an effective way to achieve drag reduction.[8,9] The streamwise vortex is the key link of the self-maintenance mechanism in TBL. From the perspective of control, a method that can manipulate streamwise vortices and impede the self-generating process is beneficial to the purpose of skin-friction drag reduction. In fact, the periodic effect of the actuator interferes with the streamwise vortex to produce the modulation effect on the coherent structure, and the drag reduction effect is realized.[10]

Active control can be categorized into two types: open-loop control and closed-loop control, based on whether the presence of a feedback sensor in the flow field.[11,12] Despite achievements obtained from experimental and numerical simulations of open-loop control,[13–16] studies of closed-loop control, especially from an experimental perspective, have been few. DNS results show that closed-loop control can effectively achieve drag reduction effect in the TBL.[17,18] Due to the intricate nature of closed-loop control, the challenges associated with precise measurement of wall skin friction, and the typically limited responsiveness of actuators, the successful implementation of closed-loop control for achieving significant drag reduction has been relatively rare.[19,20]

†Corresponding author. E-mail: nanj@tju.edu.cn

© 2024 Chinese Physical Society and IOP Publishing Ltd

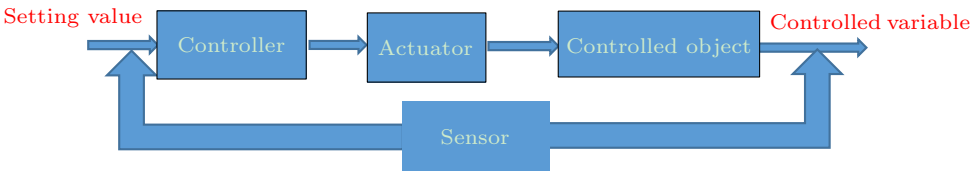


Fig. 1. Closed-loop control system.

The closed-loop control system is generally comprised of the controlled object, sensor, actuator, and controller (Fig. 1). Once the controller has received the input variable, it proceeds to utilize an appropriate control algorithm to determine the necessary operation or modulation. Subsequently, it generates an output signal that is then transmitted to the actuating mechanism. The actuating mechanism, in turn, carries out the corresponding actions of the structural actuator in order to achieve the desired active control effect.[21] The closed-loop control mainly adopts approaches such as optimal control, suboptimal control, and linear control, most of which are based on DNS.

Using the suboptimal control method, Choi *et al.*[22] achieved 16%–22% drag reduction rate based on wall pressure and friction. Bewley *et al.*[23] researched optimal control in turbulent channel flow, achieving 50% drag reduction effect. Xu Chunxiao *et al.*[24] conducted inversion control research to improve the drag reduction rate to 34% from 25%, finding the control effect on the self-sustaining mechanism in the near-wall region of the TBL. Chen Xi *et al.*[25] analyzed the mechanism of active control drag reduction techniques from the quantitative perspective, and obtained 17% drag reduction effect with 15% energy saving. Yao Jie *et al.*[26] proposed drag reduction method (composite drag control, CDC), and found the best drag reduction of about 33% at $Re_\tau \approx 180$.

The zero-net-mass-flux jet actuator is extensively utilized in the field of flow control owing to its compact structure and high degree of flexibility.[27] This phenomenon relies on the formation of counter-rotating vortex pairs along the perforation edge of the fluid. These vortex pairs are generated by intense shear forces and subsequently migrate downstream due to their own induced velocity. The migration process produces the drag reduction effect.

Luo Zhenbing[28] proposed a dual synthetic jet with two cavities, which promoted the structural development and application range of the motivator. Wang Jinjun and Feng Lihao[29] verified the efficient zero-net-mass-flux jet excitation signal proposed by Zhang and Wang[30] through cylindrical winding experiment. Liu Peiqing[31] used a PZT actuator as the synthetic jet actuator to inject the vortex structure formed under the effect of slit shear to the vortex structure, finding that the spanwise vortex generated by disturbance curbed the regeneration of near-wall turbulent structure and the skin friction in the downstream of the slit decreased. Cannata *et al.*[32] implemented a localized high-frequency disturbance on a linear synthetic jet array, perpendicular to the average incident flow. The results indicated a decrease in wall shear stress near the outlet and 20% reduction rate in turbulence decay. In a study conducted by Rathnasingham,[33] the linear control method was employed to achieve 7% drag reduction effect in resistance downstream of the actuator. Additionally, 30% decrease in streamwise velocity pulsation was observed in the TBL. Adopting the closed-loop control solution, Qiao[34] used PZT vibrators as actuators, finding the disturbance of the vibrators curbed high-speed flow events and achieved 23% drag reduction rate. Tang and Zheng *et al.*[16,35] indicated that the perturbation effect was concentrated in the inner region and the PZT actuator could provide a direct forcing input into the near-wall cycle. They proposed that the fundamental forcing frequency and associated harmonics were coupled with the innate small-scale near-wall cycle of the underlying TBL flow.

This paper presents an experimental investigation conducted in a wind tunnel, focusing on the closed-loop active control of the TBL using a zero-net-mass-flux jet. The HWA technology was utilized to implement the zero-net-mass-flux jet device, which was designed with dual PZT vibrators serving as actuators. These actuators were employed to measure the streamwise velocity signal at various normal positions in the TBL. This study mainly analyses the impact of perturbations on the multi-scale coherent structure and explores the drag reduction mechanism.

2. Experimental setup

The closed-loop control system was comprised of a hotwire probe as a sensor, a single-chip microcomputer (SCM) as a controller, and dual oscillators as the action. Meanwhile, two PZT actuators were hung in parallel and arranged along the spanwise direction.

The SCM unit was comprised of a SCM power interface 1, algorithm copy interface 2, CPU3, IFA analog voltage input interface 4, AC voltage-stabilized power input, and PZT actuators voltage input interface 5 and MOSFET pipe 6 (Fig. 2). The core component of the closed-loop control system was the SCM. Furthermore, the device was connected in parallel to a rectifying diode and a varistor. This configuration served the purpose of consuming any accumulated charge and safeguarding the MOSFET tube against breakdown caused by high voltage. Ultimately, this arrangement ensured the proper and safe

functioning of the on/off switch. The SCM control device was put in a homemade box and connected to a computer installed with a control module LabVIEWDSC for data acquisition and real-time feedback control. The data acquisition interface is shown in Fig. 3.

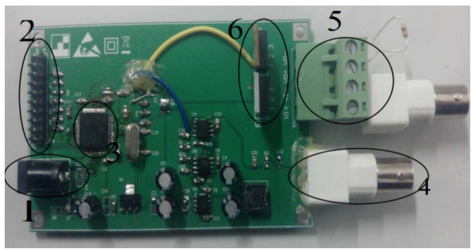


Fig. 2. Picture of the SCM unit.

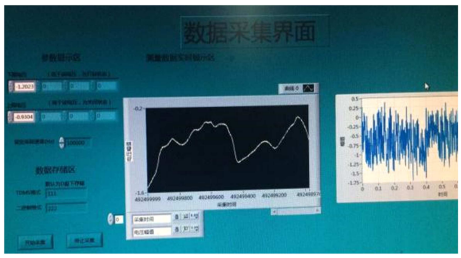


Fig. 3. Computer control interface of LabVIEW.

The closed-loop control system utilized a sensor consisting of a tungsten wire segment that was welded onto a single hot-wire probe, also known as the detection probe. The diameter of the tungsten wire was measured to be 4 μm, while its length was determined to be 1.25 mm. The actuating mechanism included a hot-wire probe, PZT activators, a controller, and a Yuanfang GK10005 AC power supply. The system's controlled object consisted of coherent structures located in the near-wall region of the TBL.

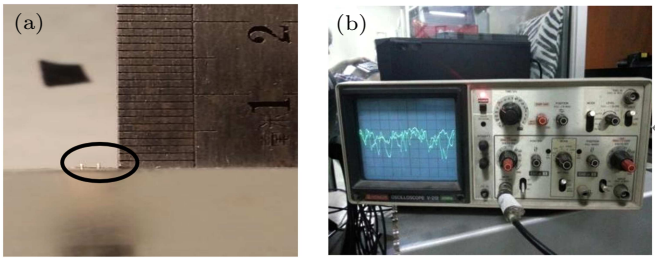


Fig. 4. Localization of the hot sensor and output voltage signal of the sensor. (a) Localization of the hot sensor. (b) Output voltage signal of the sensor.

Moin *et al.*[17] used the numerical simulation method to conduct linear closed-loop control of coherent structures, concluding that the skin friction decreases when the actuator is in the region $y^+ < 20$, while it increases in the region $y^+ > 20$. In this paper, the detection probe was placed 39.8 mm upstream of the PZT vibrators, about 0.6 mm at the normal position $y^+ = 15$. underwent precise adjustments, the location of the hot-wire sensitive filament was determined using a high-resolution camera. This meticulous process was carried out to ensure that the error remained below $5\nu/u_\tau$, as depicted in Fig. 4.

The detection probe acquired information from coherent structures in the near-wall region of the TBL upstream, and then the SCM controller identified the coherent structures. Upon detection of burst events of coherent structures, the drive circuit was promptly connected, initiating the vibration of the PZT vibrators. The mu-level method, which is widely recognized as a highly accurate mono-component technique for detecting burst events, was utilized.[36] The algorithm is as follows:

The detection function $D(t)$ of the mu-level method

$$D(t) = \begin{cases} 1, & u' < -Lu'_{\rm rms}, \\ 1, & -u'_{\rm rms} < u' < -0.25Lu'_{\rm rms} \& D(t-\Delta t) = 1, \\ 0, & u' > -0.25Lu'_{\rm rms}, \\ 0, & -Lu'_{\rm rms} < u' < -0.25Lu'_{\rm rms} \& D(t-\Delta t) = 0. \end{cases} \quad (1)$$

When $u' < -Lu'_{\rm rms}$, the jet events of low-speed fluids pass through the sensor, the controller is in the "on" state and the PZT vibrators start to vibrate to disturb burst events of coherent structures. When $u' > -0.25Lu'_{\rm rms}$, it indicates that no jet events of low-speed fluids pass through the sensor, the controller is in the "off" state and PZT vibrators do not vibrate. Specifically, u' is the streamwise pulsation velocity and $u'_{\rm rms}$ is the root-mean-square value of pulsation velocity, Δt is the time interval. The threshold L takes the value of 1.

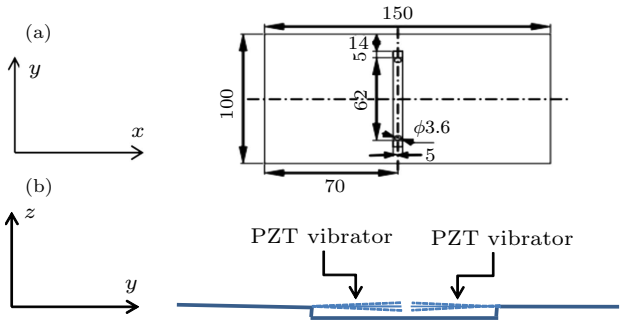


Fig. 5. The model diagram of PZT vibrators.

The actuator used in this application consisted of PZT vibrators, which were made by bonding phosphor copper and PZT ceramics together. The measured effective vibration length was 30 mm. The phosphor copper plate used in the experiment had dimensions of 3.6 mm in width and 0.22 mm in thickness. Two PZT actuators were hung in parallel and arranged along the spanwise direction, embedded in the compartment 5 mm deep of the plate. The vibration model of the PZT vibrators was the cantilever beam mode. The dual vibrators were positioned with a separation of 2 mm and maintained a 1 mm gap with the plates. This arrangement was implemented to facilitate air ventilation and prevent the PZT vibra-

tors from making contact with the wall surface, as depicted in Fig. 5.

According to the Euler–Bernoulli beam theory, the vibration mode of the PZT is a cantilever beam. If the copper pole of a vibrator and the ceramic pole of the other vibrator were connected to the same pole of the power supply, the two vibrators vibrated in opposite directions, which was called asynchronous (ASYN) vibration. The vibrators work in a synchronous (SYN) and ASYN way to introduce the perturbation into the TBL flows. A control converter that was made by the user was utilized to facilitate the transition between SYN and ASYN states.

The experiment was conducted in a low-speed reflux wind tunnel of the Fluid Dynamics Laboratory in Tianjin University. The cross section of the segment was a chamfered rectangle with the size of 1500 mm×800 mm×600 mm. The plate was placed vertically at the centerline of the experimental section, and its size was 1700 mm×600 mm×15 mm. A 2 mm diameter trip wire and sandpaper were strategically installed downstream of the plate leading edge. This setup serves to expedite the transition process and guarantee accurate measurements, ultimately achieving a fully developed state.

The experimental parameters are shown in Table 1. Here the momentum loss thickness $\theta = \int_0^\delta \frac{u}{U}[1-\frac{u}{U}]\mathrm{d}y$, ν is the kinematic viscosity coefficient, and Reynolds number $Re_\theta = \theta U_\infty/\nu$.

Table 1. Basic fluid field of properties of the TBL.

Quantity	Value
Free incoming velocity U_∞ (m·s^{-1})	9.00
Thickness of the boundary layer δ_{99} (mm)	43.00
Momentum loss thickness of boundary layer θ (mm)	4.03
Momentum loss Reynolds number Re_θ	2700

At 2 mm downstream of the PZT vibrators, the streamwise velocity signals at different normal positions of the TBL were measured by HWA. The TSI-1621A-T1.5 hot-wire probe and the detection probe can realize synchronous experimental measurement. The sampling frequency was 100 kHz, the number of samples was 2^{22} and the sampling time of a spatial point was about 42 s. The driving voltage amplitude was 100 V, and the frequency was 0 Hz, 80 Hz and 160 Hz, respectively. This study involved conducting non-control (0 V 0 Hz, where the vibrators remained inactive) and two ASYN control cases (ASYN 100 V/80 Hz and 100 V/160 Hz). The experimental setup is shown in Fig. 6.

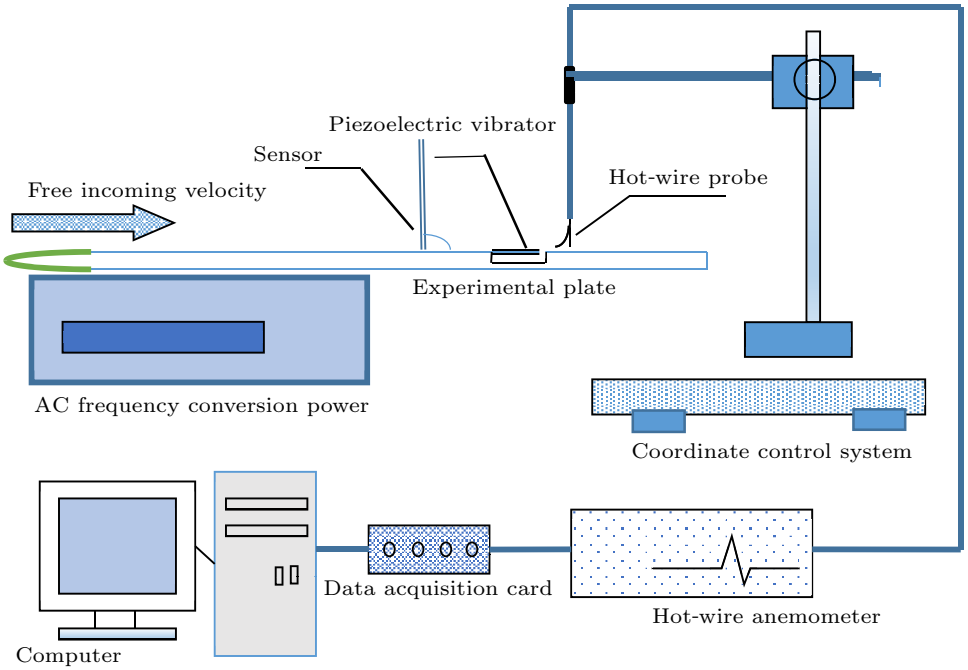


Fig. 6. Diagram of the experimental setup.

3. Experimental results

3.1. Drag reduction rate

The wall shear stress is

$$\tau_\mathrm{w} = \rho u_\tau^2, \tag{2}$$

where ρ is air density and u_τ is wall friction velocity. The wall friction velocity u_τ is solved by the method proposed by Jiang Nan.[37]

The friction factor is calculated by

$$\tau_\mathrm{w} = \frac{1}{2}C\rho U_\infty^2. \tag{3}$$

The relative drag reduction rate is

$$R = 1 - C_\mathrm{fc}/C_\mathrm{fn}, \tag{4}$$

where $C_{\rm fc}$ and $C_{\rm fn}$ are the friction factors of the control and non-control cases. The drag reduction rate of 16.7% is achieved in the ASYN 100 V/160 Hz case in Table 2.

Table 2. Drag reduction rate for each case.

Case	Wall friction velocity u_τ (m/s)	Drag reduction rate R (%)
0 V/0 Hz	0.407	–
100 V/80 Hz	0.380	12.8
100 V/160 Hz	0.371	16.7

The vibration time of the piezoelectric oscillator occupies about 25% of the total time in the closed-loop control, indicating that the energy saves about 75% and the drag reduction effect comparable to that of the open-loop control case is realized,[15] which highlights the superior performance of the closed-loop control.

3.2. Mean velocity profile

The mean velocity profiles of the TBL in different cases are presented in Fig. 7. Specifically, $y^+ = yu_\tau/\nu, u^+ = u/u_\tau$ are normal position and streamwise mean velocity nondimensionalized by u_τ and ν.

$$\frac{\Delta\tau_{\rm w}}{\tau_{\rm w}} = \frac{\Delta u_\tau^2}{u_\tau^2} = \frac{2u_\tau \Delta u_\tau}{u_\tau^2} = \frac{2\Delta u_\tau}{u_\tau} = \frac{-2\Delta b}{U^+ + \frac{1}{k}}, \tag{5}$$

where δb is the intercept of the log-law layer in the TBL and $\Delta\tau_{\rm w}/\tau_{\rm w}$ is the drag reduction rate. The above equation[36] indicates a positive correlation between $\Delta\tau_{\rm w}/\tau_{\rm w}$ and Δb, i.e., the larger the intercept of the log-law layer, the higher the drag reduction rate.

The log-law layer in the TBL satisfies the following expression:

$$u^+ = k^{-1}\ln y^+ + b, \tag{6}$$

where b is related to the wall friction velocity u_τ as the differential equation

$$\mathrm{d}u_\tau/u_\tau = -\mathrm{d}b/(u^+ + 1/k), \tag{7}$$

where $k = 0.41$ is the Karman constant. Therefore, $\mathrm{d}b$ becomes a visual measure of control effect in the TBL, i.e., the larger the intercept of the log-law layer, the higher the drag reduction rate.

Figure 7 illustrates that the log-law layer exhibits an upward trend and an increased intercept after control. This observation suggests that the disturbance caused by the PZT vibrators has a noticeable drag reduction effect on turbulent boundary layer. The upward movement is larger in the controlled case ASYN 100 V/160 Hz, resulting in a more effective control effect compared to the controlled case ASYN 100 V/80 Hz.

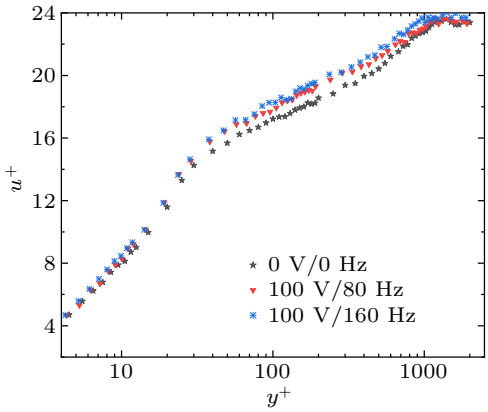


Fig. 7. Mean velocity profiles of the TBL at different cases.

The drag reduction effect in the 100 V/160 Hz case is superior, prompting a comparison between the uncontrolled case (0 V/0 Hz) and the controlled case (ASYN100 V/160 Hz). This analysis aims to further understand the modulation effect of the disturbance on the coherent structure under the closed-loop control.

3.3. Root-mean-square value and skewness factor

The root-mean-square (RMS) of the streamwise fluctuation velocity $u'_{\rm rms}$ represents the relative average energy magnitude of turbulent fluctuation. The skewness factor $S_u = \langle u'^3\rangle/\langle u'^2\rangle^{3/2}$ represents the distribution characteristics of positive and negative turbulent fluctuation. If $S_u > 0$, then the positive fluctuation velocities dominate the major part in the turbulence.

Figure 8 shows the RMS $u'_{\rm rms}$ and skewness factors S_u of streamwise fluctuation velocities in different cases. As can be seen from Fig. 8(a), the $u'_{\rm rms}$ in the near-wall region $y^+ < 60$ increases after control. The peak of $u'_{\rm rms}$ in uncontrolled case appears at $y^+ = 12$ with a maximum value of 0.50. On the other hand, the peak of $u'_{\rm rms}$ in controlled case appears at $y^+ = 19$ with a maximum value of 0.66. The observed phenomenon suggests that the vibrators generate a disturbance effect, which results in the fulfillment of energy input and subsequent amplification of energy in the TBL.

As can be seen from Fig. 8(b), the effect of disturbance on skewness factors is concentrated in the near-wall region $y^+ < 60$. In the region $y^+ < 20$ and $S_u > 0$, the skewness factor increases after control, which may be attributed to the turbulent pulsations in the extremely near-wall region subject to the strong disturbance of the PZT vibrators.

In the region $20 < y^+ < 60$ and $S_u < 0$, the skewness factor in 100 V/160 Hz case is smaller than that of the non-control case. This observation suggests that there is a decrease in the occurrence of positive high-speed fluctuations following the implementation of control measures. The production of high-speed fluids is reduced, resulting in a decrease in the downward sweep effect of these fluids. This finding aligns with the

research conducted by Bai.[38] When the PZT vibrators are positioned far from the wall, the diminishing impact of their disturbance effect can be observed.

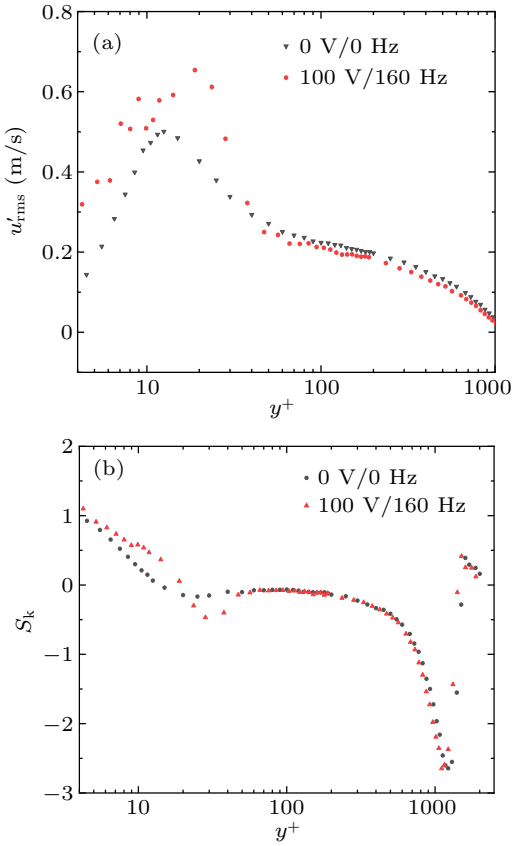


Fig. 8. Distribution of square value and skewness of fluctuations in different cases. (a) Distribution of square value in different cases; (b) skewness of fluctuations in different cases.

3.4. Filter decomposition

In order to distinguish and analyze the interactions between large-scale and small-scale fluctuations, the original fluctuation signal is decomposed using the low-pass filter method. Tang *et al.*[39] concluded that the large-scale and small-scale fluctuations and their interactions will be fairly robust when the cutoff wavelength is selected as $\lambda = 2\delta$.

Figure 9 shows the RMS distribution of large-scale and small-scale fluctuation velocities $u^+_{\rm rms}$. Figures 9(a) and 9(b) are the RMS of large-scale and small-scale fluctuations respectively. As shown in Fig. 9, the RMS of large scale decreases and small scale increases after control in the near-wall region $y^+ < 60$. The maximum RMS of large-scale before and after control is 1.71 and 1.50 at $y^+ = 32$, respectively. On the other hand, the maximum RMS of small scale before and after control is 2.51 and 2.75 at $y^+ = 28$, respectively.

The observation made in Fig. 9 indicates that the disturbance of vibrators effectively mitigates large-scale fluctuations, while simultaneously enhancing small-scale fluctuations. The observed phenomenon suggests that the disturbance amplifies the behavior of small-scale fluctuations, diminishes the strength of large-scale fluctuations, and alters the energy distribution in the near-wall region. Consequently, the energy from large-scale fluctuations is redirected towards the small-scale fluctuations, resulting in heightened turbulent dissipation and ultimately leading to the desired drag reduction effect.

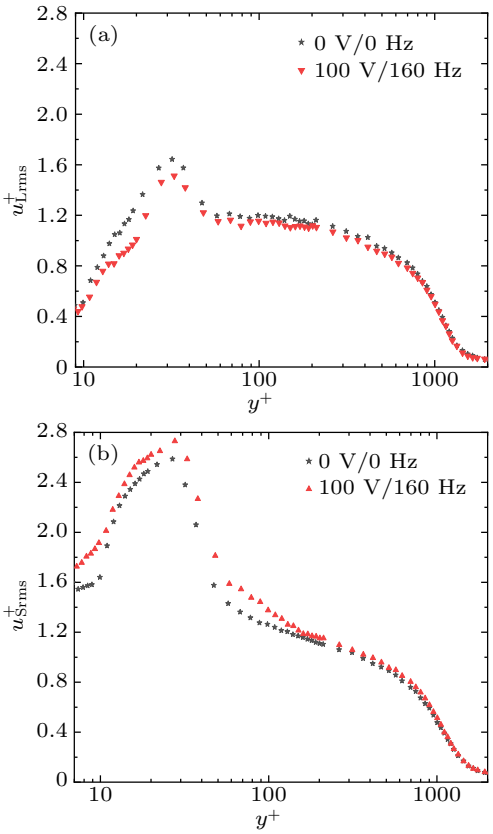


Fig. 9. Square value of large-scale and small-scale fluctuation velocity. (a) Large-scale fluctuation velocity. (b) Small-scale fluctuation velocity.

The amplitude modulation effects of the large scales were employed to observe the modulation effect.[40] This method follows the approach by Mathis *et al.*,[41] which has been widely accepted to study scale interactions in TBL flows.[42]

The Hilbert transform of the streamwise velocity signal $X(t)$ is

$$X(t) = H\{x(t)\} = \frac{1}{\pi} P \int_{-\infty}^{+\infty} \frac{x(\tau)}{t-\tau} \mathrm{d}\tau, \tag{8}$$

where P is the Cauchy principal value of the integral. $X(t)$ is the convolution of $x(t)$ and $1/\pi(t)$

$$X(t) = x(t) * (1/\pi(t)). \tag{9}$$

The Fourier transformation was performed on $1/\pi(t)$

$$H\{1/\pi(t)\} = -\mathrm{i}\,\mathrm{sgn}(\omega) = \begin{cases} -\mathrm{i} & \text{for } \omega > 0, \\ \mathrm{i} & \text{for } \omega < 0. \end{cases} \tag{10}$$

The complex analysis signal $Z(x)$ is defined associated with $x(t)$ as

$$Z(x) = x(t) + \mathrm{i}X(t) = A(t)\,\mathrm{e}^{\mathrm{i}\phi(t)}, \tag{11}$$

where $A(t)$ and $\varphi(t)$ represent the instantaneous mode and phase information respectively. $A(t)$ is represented as the envelope of the signal $x(t)$.

Turbulent fluctuation velocity signal contains a wide frequency band, and the results obtained by Hilbert transformation have not only the envelope to indicate the changing trend of pulsation signal amplitude but also the "carrier" of various small-scale pulsations. In order to eliminate this effect, we filter the obtained results with the same cutoff wavelength $\lambda = 2\delta$.

The small-scale pulsations were filtered by the Hilbert transformation, the amplitude envelope of small-scale fluctuations was derived using Hilbert conversion in conjunction with filter decomposition. The subsequent calculation yielded the correlation coefficient, denoted as C_{R}, between the velocity signals of large-scale and small-scale fluctuations

$$C_{\mathrm{R}} = \langle u'^{+}_{\mathrm{L}} E_{\mathrm{L}}(u_{\mathrm{s}})^{+} \rangle / \sqrt{\langle u'^{+}_{\mathrm{L}} \rangle^{2} \langle E_{\mathrm{L}}(u_{\mathrm{s}})^{+2} \rangle}, \tag{12}$$

where $\sqrt{u_{\mathrm{L}}^{+2}}$ is the RMS value of the large-scale pulsations, $E_{\mathrm{L}}(u_{\mathrm{s}})$ is the large-scale fluctuations of the small-scale envelope, $E_{\mathrm{L}}(u_{\mathrm{s}})^{+}$ is the characteristic representation of the dimensionless small-scale pulsation amplitude for each instantaneous value. This coefficient C_{R} represents the effects of modulation and amplitude modulation exerted by large-scale structures on small-scale structures.[43]

Figure 10 presents the correlation coefficients of large- and small-scale fluctuations, where the horizontal axis is the normal position y^{+} and the vertical axis is the correlation coefficient C_{R}. The correlation coefficient in the viscous sublayer region demonstrates a notable elevation in the non-control case, as depicted in Fig. 10. The peak value of C_{R} is 0.10 in the uncontrolled case, while it is 0.36 after control at $y^{+} = 25$. This elevation gradually diminishes as the normal position increases and eventually stabilizes in the log-law layer.

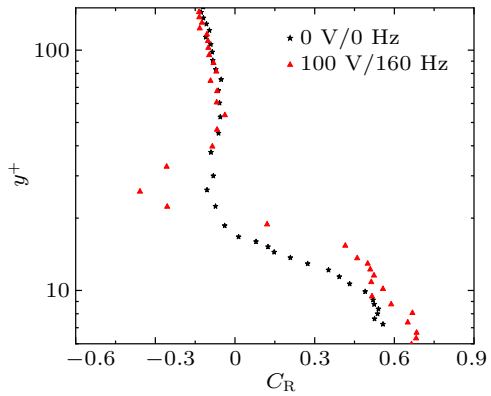


Fig. 10. Correlation coefficients of large-scale fluctuation and small-scale amplitude.

The observed phenomenon suggests that the modulation effect is prominent in the viscous sublayer and log-law layer, but diminishes gradually as the distance from the wall increases. After implementing control measures, the correlation coefficient in the viscous sublayer region experiences an increase and demonstrates a robust positive correlation. The observed phenomenon suggests that the presence of large-scale structures significantly influences the behavior of small-scale structures through the perturbation caused by the PZT vibrators.

3.5. Wavelet analysis

The main characteristics of wavelet transform are multi-scale and localization, which is a more efficient way to acquire the detail turbulence information at different scales.[14] The wavelet coefficient has the ability to localize the turbulent details in the temporal domain at a certain scale but the local events in time domain cannot be recognized by FFT.

The wavelet coefficient $W_u(a,s)$ was obtained by wavelet decomposition of the streamwise velocity signal $x(t)$, The energy of signal $x(t)$ can be determined by performing wavelet decomposition at various scales and summing the total energy across all scales.[44]

For a given one dimensional velocity $u(t)$, its wavelet coefficient $W_u(a,s)$ under the wavelet function $W_{as}(t)$ is defined as

$$W_u(a,s) = \int_{-\infty}^{+\infty} u(t) \overline{W_{as}(t)} \, \mathrm{d}t, \tag{13}$$

where the family of wavelet functions $W_{as}(t)$ is obtained by translating and stretching the wavelet generating function $W(t)$, respectively, for time b and scale a, i.e.,

$$W_{as}(t) = \frac{1}{\sqrt{a}} W\left(\frac{t-s}{a}\right). \tag{14}$$

The energy conservation law is written as follows:

$$\int_{-\infty}^{+\infty} |u(t)|^2 \, \mathrm{d}t = \int_{0}^{+\infty} \frac{E(a)}{a^2} \, \mathrm{d}a, \tag{15}$$

where

$$E(a) = \frac{2}{C_W} \int_{-\infty}^{+\infty} |W_u(a,s)|^2 \, \mathrm{d}s, \tag{16}$$

$$C_W = \int_{-\infty}^{+\infty} \frac{|W(\omega)|^2}{\omega} \, \mathrm{d}\omega < \infty, \tag{17}$$

in which $W(\omega)$ is the Fourier transform of the wavelet generating function $W(t)$.

There must be a maximum scale $r = a^{*}$ that contains the most kinetic energy among all the scales. The maximum energy criterion of wavelet decomposition can be used to determine the time scales of the coherent structures.[45] In this study, the Daubechies 2 (db2)[43] wavelet was chosen as the mother wavelet for the purpose of decomposing the streamwise velocity signal into 21 scales at each space point. The scaling factor in the given text is denoted by the variable "a".

The auto-correlation analysis of wavelet coefficients demonstrates the relationship between the burst frequency f and the wavelet decomposition scale a, as depicted in Fig. 11. Figure 11 illustrates the burst frequency in the non-control case. The burst frequency is observed to be 178 Hz, which

corresponds to the maximum energy scale (8th scale). Additionally, a burst frequency of 86 Hz is observed, corresponding to the 9th scale. Therefore, the frequency of 178 Hz closely aligns with the disturbance frequency of 160 Hz, which corresponds to the maximum energy scale. As a result, it exhibits a more pronounced drag reduction effect.

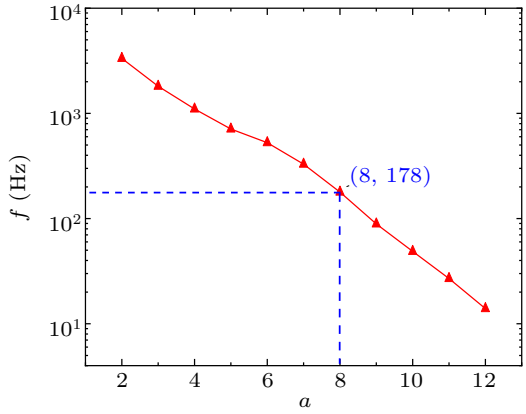


Fig. 11. Relation between wavelet scale and corresponding frequency.

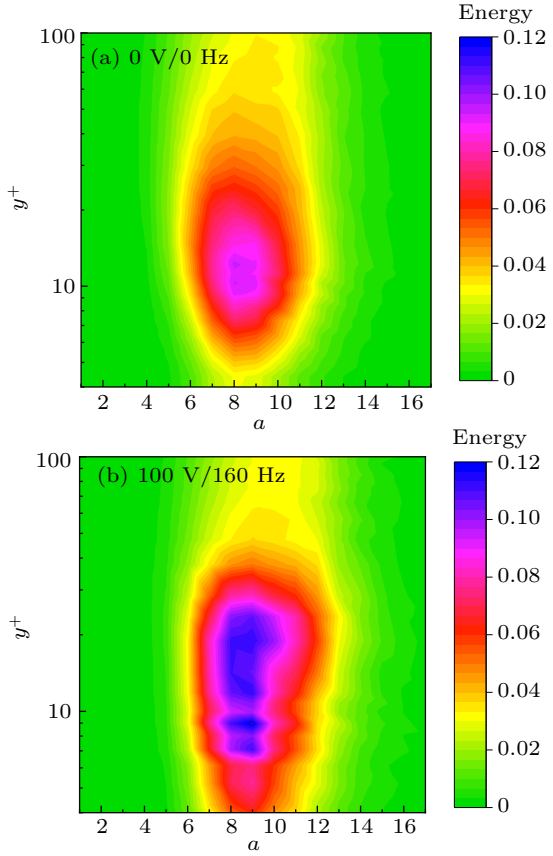


Fig. 12. Energy cloud distribution in different cases. (a) 0 V/0 Hz; (b) 100 V/160 Hz.

Figure 12 shows the energy cloud distribution in different cases. The vertical axis is the normal position y^+, the horizontal axis is the scale a and different colors present the energy value. As seen from Fig. 12, there is a noticeable trend of shifting towards the 9th scale in the controlled scenarios. The maximum value of energy is 0.095 and 0.122 before and after control, respectively. The energy value experiences a substantial increase in the controlled case. The energy is concentrated in the 7–10 scale range around the energy maximum scale.

The disturbance of the PZT vibrators decreases the energy of large-scale coherent structures and increases the energy of small-scale coherent structures, indicating a decrease in the generation of turbulence and the enhancement in the dissipation of turbulence. The augmentation of turbulence dissipation impacts the amplification of the low-speed streak and facilitates the transition of turbulent flow towards a more laminar state.[45] The vibration scale exhibits a significant interaction with another scale, thereby influencing the modulation of the kinetic energy cascade mechanism in the near-wall region.

In the mu-level method, mark time t is in the burst event when $u' < -Lu'_{\rm rms}$, mark time t is not in the burst event when $u' > -0.25Lu'_{\rm rms}$. Whether time t is in the burst event according to the state of the previous moment $t-\Delta t$, if $t-\Delta t$ is in the burst event, then mark t is in the burst event, otherwise, mark t is not in the burst event. The average duration of burst event is indicated by the time between the leading and posterior edges of successive burst events. The burst period is the time interval between the leading edges between two consecutive burst events.[46]

Figure 13 shows the average duration, mean intensity of burst events and the proportion of burst time in a burst period in controlled and uncontrolled cases. Figure 13 demonstrates that after implementing control measures, there is a noticeable decrease in the average duration time, mean intensity, and proportion of burst time. Additionally, the burst events are effectively suppressed. This observation indicates that the disturbance caused by the oscillators disrupts the streamwise vortex structure, which is closely associated with high skin friction. Consequently, this perturbation leads to the desired outcome of reducing drag.

Combined with the above conclusion, it can be seen that the disturbance mainly conducts energy to the vibration scale and small scale, but weakens the intensity of the large scale. The disturbance generated by PZT oscillators has the characteristics of stable periodicity, positive and negative symmetry, low intermittency, and high pulsation strength. Additionally, it achieves a drag reduction effect similar to that of the open-loop control case, highlighting the superior performance of the closed-loop control.

The method of extrema of wavelet coefficients was applied to extract the conditional phase-averaged waveforms of burst events. The occurrence of sweep events was determined by the positive maximum of wavelet coefficient. The conditional phase-averaged waveforms of sweep events at the 8th scale were obtained in various cases, as depicted in Fig. 14. The horizontal axis is time t, the vertical axis is the fluctuation velocity of the burst event. Figures 14(a) and 14(b) present

a comparison at different normal positions in non-control and 100 V/160 Hz control case. As shown in Fig. 14, the fluctuation amplitude increases after control in the near-wall region. The maximum fluctuation amplitude is 0.261 and 0.294 before and after control at $y^+ = 11$. This phenomenon implies that the turbulent kinetic energy of small scale is enhanced and the random coherent structure becomes more orderly after control.[16] The energy consumed by the friction between the small-scale high-speed fluid and the wall decreases, thus the average kinetic energy increases. The increase in fluctuation amplitude observed suggests that the disturbance caused by the PZT vibrators has a modulating effect on coherent structures, resulting in modulation and amplitude modulation effects.

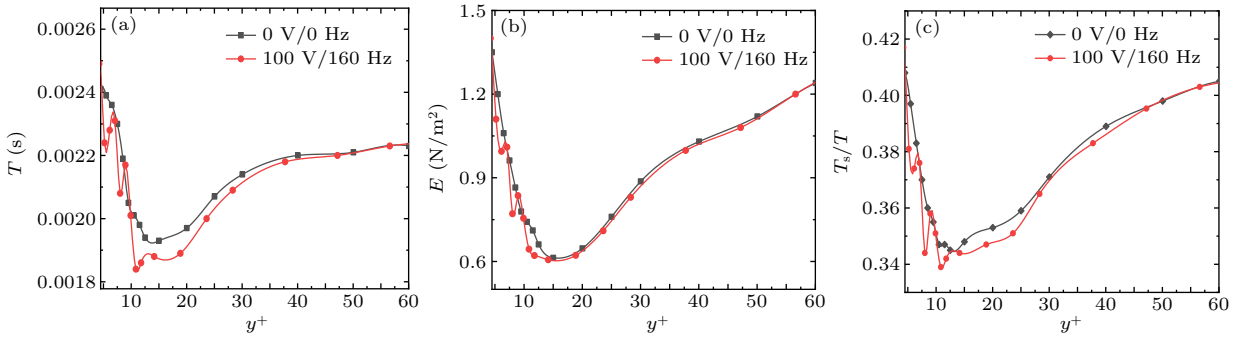


Fig. 13. Burst events in different cases. (a) Average duration of burst events; (b) mean intensity of burst events; (c) proportion of burst time.

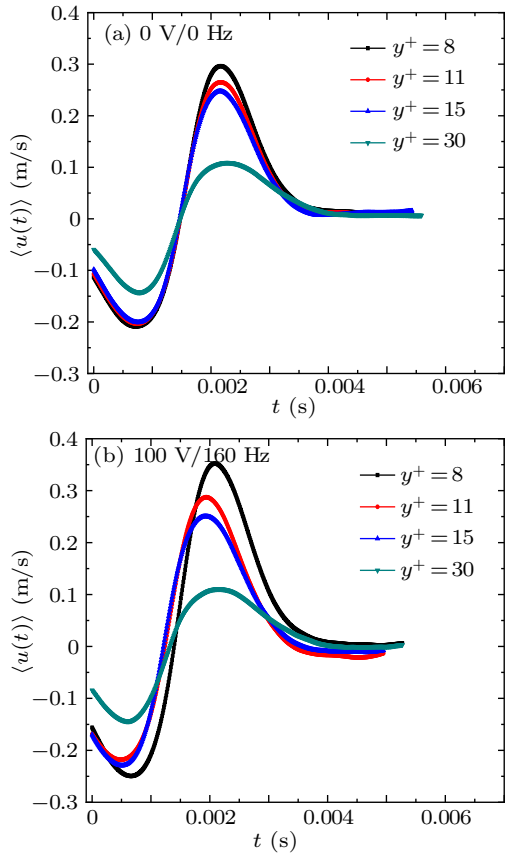


Fig. 14. Conditional phase-averaged waveforms of sweep events. (a) 0 V/0 Hz; (b) 100 V/160 Hz.

4. Conclusion

The zero-net-mass-flux active control experiment was conducted by HWA technology. A variable-frequency AC supply was used to control voltage and frequency of the PZT oscillators, which were employed to interfere with and modulate the coherent structures in the TBL via the ASYN vibration. The primary findings can be summarized as follows:

(1) The drag reduction rate of 16.7% was obtained comparable to that of the open-loop control and saved 75% of the energy input at the ASYN 100 V/160 Hz closed-loop control case. The 160 Hz case achieves more effective control effect than 80 Hz case.

(2) The RMS $u'_{\rm rms}$ in the near-wall region increased after control. The vibration produces energy input, high-speed fluids are inhibited in the region $20 < y^+ < 60$.

(3) The near-wall region experiences a significant modulation effect on small-scale structures due to the presence of large-scale structures. The burst events are suppressed in the near-wall region after control.

(4) The modulation effect on coherent structures is produced by the disturbance. The energy distribution within the near-wall region of the TBL undergoes alteration.

Acknowledgements

Project supported by the National Natural Science Foundation of China (Grant Nos. 12202309, 1233000165, 12172242, and 12272265), Science and Technology Program of Gansu Province of China (Grant No. 22JR5RA304), and Tianjin Research Innovation for Postgraduate Students (Grant No. 22KJ049).

References

[1] Marusic I, McKeon B J, Monkewitz P A and Nagib H M 2010 *Phys. Fluids* **22** 065103
[2] Marusic I, Mathis R and Huchins N 2010 *Science* **329** 193
[3] Ganapathisubramani B, Hutchins N, Monty J P, Chung D and Marusic I 2012 *J. Fluid Mech.* **712** 61
[4] Guala M, Metzger M and McKeon B J 2011 *J. Fluid Mech.* **666** 573
[5] Hwang J and Sung H J 2017 *J. Fluid Mech.* **829** 751

[6] Wu D, Wang J J, Cui G Y and Pan C 2020 *Sci. China Ser. E-Tech. Sc.* **63** 214
[7] Gruncell B R K, Sandham N D and Mchale G 2013 *Phys. Fluids* **25** 043601
[8] Liu C and Gayme D F 2020 *J. Fluid Mech.* **888** A32
[9] Xu C X 2015 *Adv. Mech.* **45** 201504
[10] JimeNez J, Kawahara G, Simens M P, Nagata M and Shiba 2005 *Phys. Fluids* **17** 015105
[11] Kim K and Sung H J 2006 *J. Fluid Mech.* **557** 423
[12] Kasagi N, Suzuki Y and Fukagata K 2009 *Annu. Rev. Fluid Mech.* **41** 231
[13] Kametani Y, Fukagata K, Orlu R and Schlatter P 2015 *Int. J. Heat. Fluid Fl.* **55** 132
[14] Mitchell L, Flint O, Thomas and Stanislav G 2023 *Int. J. Heat. Fluid Fl.* **103** 109194
[15] Bai J X, Jiang N, Zheng X B, Tang Z Q, Wang K J and Cui X T 2018 *Chin. Phys. B* **27** 074701
[16] Zheng X B, Jiang N and Zhang H 2015 *Chin. Phys. B* **24** 064702
[17] Hammond E P, Bewley T R and Moin P 1998 *Phy. Fluids* **10** 2421
[18] Kim J and Bewley T R 2007 *Annu. Rev. Fluid Mech.* **39** 383
[19] Rebbeck H and Choi K S 2006 *Phys. Fluids* **18** 175
[20] Qiao Z X, Wu Z and Zhou Y 2018 *Phys. Fluids* **30** 11
[21] Brunton S L and Noack B R 2015 *Appl. Mech. Rev.* **67** 050801
[22] Kang S and Choi H 2000 *Phys. Fluids.* **12** 3301
[23] Bewley T R, Moin P and Temam R 2009 *J. Fluid Mech.* **447** 179
[24] Deng B Q and Xu C X 2012 *J. Fluid Mech.* **710** 234
[25] Chen X, Yao J and Hussain F 2021 *Phys. Rev. Fluids* **6** 013902
[26] Yao J, Chen X and Hussain F 2021 *Phys. Rev. Fluids* **6** 054605
[27] Qu L H and He X 2019 *J. Fluid Mech.* **880** 764
[28] Luo Z B, Xia Z X and Liu B 2006 *J. AIAA* **44** 2418
[29] Wang J J, Feng L H and Xu C J 2007 *Sci. China Ser. E-Tech. Sci.* **50** 550
[30] Zhang P F and Wang J J 2007 *J. AIAA* **45** 1058
[31] Guo H, Huang Q M, Liu P Q and Qiu L 2015 *Fluid Dyn. Res.* **47** 045501
[32] Cannata M, Cafiero G and Iuso G 2020 *J. AIAA* **58** 2042
[33] Rathnasingham R and Breuer K S 2013 *J. Fluid Mech.* **495** 209
[34] Qiao Z X, Zhou Y and Wu Z 2017 *Proc. R. Soc. A* **473** 20170038
[35] Tang Z Q and Jiang N 2020 *Phys. Fluids* **32** 015110
[36] Tubergen R G and Tiederman W G 1993 *Exp. Fluids* **15** 255
[37] Fan X and Jiang N 2005 *Eng. Mech.* **01** 28
[38] Bai H L, Zhou Y, Zhang W G, Xu S J, Wang Y and Antonia R A 2014 *J. Fluid Mech.* **750** 316
[39] Tang Z Q, Jiang N, Zheng X B and Wu Y H 2016 *Exp. Fluids* **57** 1
[40] Tang Z, Jiang N, Zheng X and Wu Y 2019 *Phys. Fluids* **31** 025120
[41] Mathis R, Hutchins N and Marusic I 2009 *J. Fluid Mech.* **628** 311
[42] Jacobi I and McKeon B J 2017 *J. Turbul.* **18** 1120
[43] Mallat S and Hwang W L 1992 *IEEE. T. Inform. Theory* **38** 617
[44] Bai J X, Huang Y X, Jiang N, Ma X Y and Tang Z Q 2020 *J. Hydrodyn.* **32** 747
[45] Liu J H, Jiang N, Wang Z D and Shu W 2005 *Appl. Math. Mech.* **26** 456
[46] Metzger M and McKeon B 2010 *Physica D* **239** 1296